

Pulsars versus Dark Matter

Interpretation of ATIC/PAMELA

Dmitry Malyshev,^{*} Ilias Cholis,[†] and Joseph Gelfand[‡]

Center for Cosmology and Particle Physics

4 Washington Place, Meyer Hall of Physics,

NYU, New York, NY 10003

(Dated: November 28, 2019)

In this paper, we study the flux of electrons and positrons injected by pulsars and by annihilating or decaying dark matter in the context of recent ATIC, *PAMELA*, *Fermi*, and HESS data. We review the flux from a single pulsar and derive the flux from a distribution of pulsars. We point out that the particle acceleration in the pulsar magnetosphere is insufficient to explain the observed excess of electrons and positrons with energy $E \sim 1$ TeV and one has to take into account an additional acceleration of electrons at the termination shock between the pulsar and its wind nebula. We show that at energies less than a few hundred GeV, the expected flux from a continuous distribution of pulsars provides a good approximation to the expected flux from pulsars in the ATNF catalog. At higher energies, we demonstrate that the electron/positron flux measured at the Earth will be dominated by a few young nearby pulsars, and therefore the spectrum would contain bump-like features. We argue that the presence of such features at high energies would strongly suggest a pulsar origin of the anomalous contribution to electron and positron fluxes. The absence of features either points to a dark matter origin or constrains pulsar models in such a way that the fluctuations are suppressed. Also we derive that the features can be partially smeared due to spatial variation of the energy losses during propagation.

PACS numbers: 97.60.Gb, 95.35.+d, 96.50.S-, 98.70.Sa

Contents		B. Spatial variation in energy losses	15
I. Introduction	2	C. Constraining pulsars and ISM properties	16
II. Single pulsar flux	3	References	19
A. Properties of the interstellar medium	3		
B. Green function for diffusion-loss propagation	4		
C. Flux from a single pulsar	4		
III. Flux from a collection of pulsars	6		
A. Flux derivation	6		
B. Statistical cutoff	8		
IV. Flux from Dark Matter	9		
V. Conclusions	11		
A. Review of pulsars	12		

^{*}Electronic address: dm137@nyu.edu; On leave of absence from ITEP, Moscow, Russia, B. Cheremushkinskaya 25

[†]Electronic address: ijc219@nyu.edu

[‡]Electronic address: jg168@astro.physics.nyu.edu; National Science Foundation Astronomy and Astrophysics Postdoctoral Fellow

I. INTRODUCTION

The nature of dark matter (DM) remains one of the most interesting problems in cosmology and astrophysics. Recently, several cosmic ray experiments reported higher than expected fluxes of electrons and positrons at energies between 10 GeV and 1 TeV [1, 2, 3, 4, 5]. One interpretation is that this excess is a result of DM annihilation or decay [6, 7, 8, 9, 10, 11, 12, 13]. Standard astrophysical sources, such as pulsars [14, 15, 16, 17, 18, 19], are also a viable possibility. The main purpose of this work is to identify an observational signature which might differentiate between these two models.

Pulsars are known to produce and accelerate electrons and positrons in their magnetosphere [20]. However, as we will argue below, this acceleration is insufficient to explain the observed excess. Moreover, the spectrum of particles in the magnetosphere is further modified at the termination shock between the pulsar and the interstellar medium (ISM) or the the supernova remnant (SNR) which may contain the pulsar wind nebula (PWN). It is important to emphasize that termination shocks are observed around middle-aged pulsars (e.g. Geminga [21, 22], PSR J1747-2958 [23]) and not just young pulsars like the Crab. Most young energetic pulsars are also surrounded by a PWN (for a review see, e.g., [24]) which is powered by the continuous emission from the pulsar and remains inside the shell or envelope produced by the initial explosion (a discussion of various regions surrounding a pulsar can be found in, e.g., [25]). Inside a PWN, the electrons and positrons are confined by the nebula's magnetic field for a long period of time before escaping into the ISM. Since a pulsar loses the vast majority of the spin-down energy while its PWN still exists, we assume that most of the electrons and positrons injected by pulsars spend a significant amount of time inside a PWN before reaching the ISM. This has two main consequences:

- The spectrum of electrons and positrons injected by a pulsar into the surrounding ISM is not the spectrum of particles inside the magnetosphere (as assumed by many authors, e.g [16, 18, 26]), but the spectrum of particles that escape the PWN into the surrounding ISM. In this paper, we assume that this is the same as the electron/positron spectrum inside the PWN when it is disrupted, which we estimate using the observed broadband spectrum of these objects.

- Since the lifetime of a PWN ($t \ll 100$ kyr; [24]) is generally much smaller than the typical propagation time ($t > 100$ kyr), the electrons observed at the Earth come from PWNe that no longer exist, whereas electrons inside existing PWNe cannot reach us. Since the variability of PWNe properties is very large, we cannot predict the electron flux from a pulsar that has already lost its PWN, even if we fully know its current properties (e.g age, position, spin-down luminosity).

Therefore, the best one can do is to use the currently observed PWNe to derive a statistical distribution of their properties. This distribution can be used to either find the average flux of electrons expected from pulsars or, by assigning the PWNe random properties according to the distribution, the typical electron flux observed on Earth from all pulsars.

The observed spectrum on Earth of electrons and positrons injected by pulsars is also strongly dependent on propagation effects. In particular, the observed cutoff in the flux of electrons from a pulsar can be much smaller than the injection cutoff due to energy losses (“cooling”) during propagation. We define the cooling break, $E_{\text{br}}(t)$, as the maximal energy electrons can have after propagating for time t . Since – as stated above – the typical electron propagation time is much larger than the lifetime of a PWN, we can assume that a pulsar is a delta-function source $Q \sim \delta(t)$ and the propagation time for electrons from this pulsar can be estimated by the pulsar's age t . If the cooling break is at a lower energy than the injection cutoff from a PWN, $E_{\text{br}}(t) < E_{\text{inj}}$, then the observed break is the cooling break which depends on the age of the pulsar but is independent of the injection cutoff. Since the cooling break is much steeper than the injection break, the existence of several pulsars with $E_{\text{br}} \ll E_{\text{inj}}$ sufficiently close to the Earth such that the propagation time of electrons they inject into the ISM is less than their age will result in a sequence of steps or bumps in the spectrum. At high energies, only a few pulsars will satisfy this criteria, so these steps are expected to be well separated and therefore observable. At lower energies, we expect many pulsars to contribute, causing these steps to be averaged together and resulting in a smooth spectrum. We argue that the presence of significant steps, or bumps, in the electron spectrum at high energies would strongly suggest this excess is generated by pulsars, since the flux from the dark matter is expected to be smooth with a single cutoff. If these

features are not observed, a pulsar explanation of the observed excess is possible if there are no young energetic pulsars in the vicinity of the Earth with $E_{\text{br}} \ll E_{\text{inj}}$ [27] or there are considerable spatial variations in the energy losses of these particles as they diffuse through the ISM. The amplitude of these fluctuations also depends on the relative contributions of the backgrounds and the pulsars. If backgrounds dominate at high energies, these fluctuations may be undetectable.

This paper is organized as follows: In Sec. II, we review the propagation of electrons in the ISM. We estimate the typical propagation time and distance for electrons and positrons of a given energy and show that injection of electrons and positrons by a pulsar can be approximated by delta-functions in space and time. Using the properties of pulsars and their PWN derived in App. A, we derive the temporal evolution of the observed flux from a single pulsar at a given distance. In Sec. III, we study the flux from a distribution of pulsars, calculating the average expected flux and comparing this result to the estimate flux from pulsars in the ATNF catalog [28] – demonstrating that at energies $E \lesssim 300$ GeV this flux is well approximated by the average curve while at higher energies there are significant deviations and bump-like features due to the cooling breaks. We then compare both spectra with the ATIC, *Fermi*-LAT, and *PAMELA* data. In Sec. IV, we review the flux from dark matter. In Sec. V, we present our conclusions. We argue that the flux from dark matter is likely indistinguishable from the flux from a single pulsar or from a continuous distribution of pulsars. Thus, unless there are additional features at high energies that point to the contribution from several pulsars, it may be impossible to tell whether the excess is due to dark matter or pulsars.

The paper also contains a few appendices: in App. A we give a general review of pulsars and pulsar wind nebulae. In App. B we derive the smearing of the cooling breaks due to spatial variability of energy losses. In App. C we study some constraints that current electron and positron data put on the pulsar models.

II. SINGLE PULSAR FLUX

The flux of cosmic ray electrons at the Earth depends on both the spectrum of injected electrons and the properties of the ISM. First, we review the propagation of electrons in the ISM, and then derive the expected flux from pulsars and dark matter.

A. Properties of the interstellar medium

The ISM contains a magnetic field with a strength on the order of $3\mu\text{G}$ [29]. Since the corresponding Larmor radius for a 1 TeV electron is small, $r_L = \frac{pc}{eB} < 10^{-3}$ pc, electrons are expected to mostly follow the ISM's magnetic field lines. Because the ISM magnetic field has random fluctuations, electrons propagate along on a random path. The corresponding diffusion coefficient for relativistic particles is [30]

$$D(E) = D_0 \left(\frac{E}{E_0} \right)^\delta, \quad (1)$$

where $\delta = 0.3 - 0.6$ and $D_0 = (3 - 5) \times 10^{28} \text{cm}^2 \text{s}^{-1}$ for $E_0 = 1$ GeV. (The typical mean free path for a 1 TeV electron $r_f \sim D(E)/c > 1$ pc is much larger than the Larmor radius $r_L < 10^{-3}$ pc.) We find it convenient to express the diffusion coefficient in terms of the energy rather than the magnetic rigidity, $R \equiv p/q$, where p is the momentum and q is the charge of the particle. In our case, the two definitions are equivalent.

As electrons propagate in the ISM, they lose energy. For electrons with energy $E \gtrsim 5$ GeV, the dominant loss mechanisms are synchrotron radiation and inverse Compton scattering off Cosmic Microwave Background (CMB), infrared (IR), and starlight photons. The corresponding energy losses are

$$\dot{E} \equiv -b(E) = -b_0 E^2, \quad (2)$$

where $b_0 = 1.6 \times 10^{-16} \text{GeV}^{-1} \text{s}^{-1}$ for the local density of photons [31] and $B = 3 \mu\text{G}$. Before we present a formal solution to the propagation equations, we define a few characteristic numbers. In estimations, it is convenient to represent the parameters in the units of $\text{pc} = 3 \times 10^{18} \text{cm}$ and $\text{kyr} = 3 \times 10^{10} \text{s}$. In this paper we will usually use $b_0 = 1.6 \times 10^{-16} \text{GeV}^{-1} \text{s}^{-1} = 5 \times 10^{-6} \text{GeV}^{-1} \text{kyr}^{-1}$ and $D_0 = 3 \times 10^{28} \text{cm}^2 \text{s}^{-1} = 100 \text{pc}^2 \text{kyr}^{-1}$ with $\delta = 0.4$.

By integrating Eq. (2), we find the energy loss in terms of the electron travel time is

$$\frac{1}{E_1} - \frac{1}{E_0} = b_0 t, \quad (3)$$

where E_0 is the initial energy of the electron and E_1 is the energy at time t . The *cooling break*, defined as the maximal energy an electron can have after traveling for time t , is

$$E_{\text{br}} = \frac{1}{b_0 t}. \quad (4)$$

The characteristic travel time is therefore

$$t \gtrsim 100 \text{ kyr} \quad \text{for} \quad E \lesssim 2 \text{ TeV}. \quad (5)$$

The characteristic distance an electron travels before cooling to energy E is the diffusion distance $x_{\text{diff}}^2 = 4D(E)t$, where $t = \frac{1}{b_0 E}$,

$$x_{\text{diff}} \lesssim 5 \text{ kpc} \quad \text{for} \quad E \gtrsim 10 \text{ GeV}. \quad (6)$$

B. Green function for diffusion-loss propagation

In general, the evolution of the energy density ρ of electrons moving in random paths and losing energy can be described by the following diffusion-loss equation [29][32]

$$\frac{\partial \rho}{\partial t} = \frac{\partial}{\partial E} (b(E)\rho) + \frac{\partial}{\partial x^i} (D(E) \frac{\partial}{\partial x^i} \rho) + Q(\mathbf{x}, E, t), \quad (7)$$

where $Q \equiv dN/(dE dt d^3x)$ is the energy density of electrons injected by the source. In principle, one can also take into account re-acceleration, convection, and decays (collisions), but for electrons with $E > 10 \text{ GeV}$ these contributions can be ignored.

The general solution to Eq. (7) is found in [32][33]. To solve Eq. (7) for a general source, one introduces the Green function $G(\mathbf{x}, E, t; \mathbf{x}_0, E_0, t_0)$ which satisfies

$$\frac{\partial G}{\partial t} - \frac{\partial}{\partial E} (b(E)G) - D(E) \frac{\partial^2 G}{\partial x^2} = \delta(\mathbf{x} - \mathbf{x}_0) \delta(E - E_0) \delta(t - t_0). \quad (8)$$

Then, the solution to (7) is

$$\rho(\mathbf{x}, E, t) = \int d^3 \mathbf{x}_0 \int dE_0 \int dt_0 G(\mathbf{x}, E, t; \mathbf{x}_0, E_0, t_0) \cdot Q(\mathbf{x}_0, E_0, t_0). \quad (9)$$

The Green function can be derived as follows. One can define the variables $t' = t - \tau$ and λ [32][33], where

$$\tau \equiv \tau(E, E_0) = \int_E^{E_0} \frac{dE'}{b(E')}, \quad (10)$$

$$\lambda \equiv \lambda(E, E_0) = \int_E^{E_0} \frac{D(E') dE'}{b(E')}. \quad (11)$$

The variable $t'(t, E)$ is invariant with respect to the differential operator $\partial_t - b(E)\partial_E$. In fact, $D^{-1}(E)(\partial_t - b(E)\partial_E) = \partial_\lambda$ and Equation (8) becomes the usual diffusion equation in λ and \mathbf{x} . The Green function is then [32][33]

$$G(\mathbf{x}, E, t; \mathbf{x}_0, E_0, t_0) = \frac{1}{b(E)} \frac{1}{(4\pi\lambda)^{3/2}} e^{-\frac{(\mathbf{x}-\mathbf{x}_0)^2}{4\lambda}} \cdot \delta(t - t_0 - \tau) \theta(E_0 - E). \quad (12)$$

Eq. (7) and the above Green function have a few limitations. Both the ISM magnetic field and density of IR and starlight photons vary in space. Consequently the diffusion coefficient and the energy loss function depend on the coordinates: $D = D(E, \mathbf{x})$, $b = b(E, \mathbf{x})$, and there is no simple analytic solution to Eq. (7). In App. B we calculate corrections to the predicted e^+e^- spectrum at the Earth due to spatial variations in the energy loss function.

C. Flux from a single pulsar

With the general Green function in hand, one can find the density of electrons at any point in space for any source. In this Section, we derive the expected flux of electrons and positrons produced by a single pulsar.

The distances to pulsars are sufficiently large that we can assume that pulsars are point sources. We also assume that most of the pulsars' rotational energy is lost via magnetic dipole radiation [34] which eventually transforms into the energy of electrons and positrons

$$Q_{\text{pulsar}}(\mathbf{x}, E, t) = Q(E) \frac{1}{\tau} \left(1 + \frac{t}{\tau}\right)^{-2} \theta(t) \delta(\mathbf{x}), \quad (13)$$

where t is the pulsar age and \mathbf{x} is its position. $\theta(t)$ is the step function that ensures $Q_{\text{pulsar}} = 0$ for $t < 0$. Note that the pulsar spin-down time scale τ in this formula and the variable introduced in (10) are unrelated. We review the derivation of this formula in App. A.

At late times ($t \gg \tau$), the spin-down luminosity scales as t^{-2} . Consequently, most of the energy is emitted during $t \sim \tau$. The pulsar spin-down time scale, $\tau \lesssim 10 \text{ kyr}$, is much smaller than the typical electron propagation time, $t \gtrsim 100 \text{ kyr}$. Consequently, we can take the limit $\tau \rightarrow 0$, which results in

$$\frac{1}{\tau} \left(1 + \frac{t}{\tau}\right)^{-2} \theta(t) \Big|_{\tau \rightarrow 0} \longrightarrow \delta(t). \quad (14)$$

For pulsars with a significant PWN, the time dependence in Eq. (13) does not describe the escape of electron and positrons from the PWN into the ISM. However, for most pulsars the lifetime of the PWN ($t \lesssim 20 \text{ kyr}$; [24]) is much smaller than the typical propagation time $t \gtrsim 100 \text{ kyr}$ (Eq. (5)). Thus, the detailed time dependence of the escape is not significant and the delta-function approximation in Eq. (14) is still valid.

We assume that the energy spectrum of particles injected into the ISM $Q(E)$ by a given pulsar has the form

$$Q(E) = Q_0 E^{-n} e^{-\frac{E}{M}}, \quad (15)$$

where n is the injection index and M is the injection cutoff. We denote the initial rotational energy of the pulsar by W_0 and define η to be the fraction of this energy deposited in the ISM as e^+e^- . The total energy emitted in e^+e^- is then

$$\int Q(E)E dE = \eta W_0. \quad (16)$$

For $n < 2$, this gives

$$Q_0 = \frac{\eta W_0}{\Gamma(2-n)M^{2-n}}. \quad (17)$$

The index n and the cutoff M of the electron spectrum can be derived from the broadband spectrum of a PWN, and may vary significantly between pulsars. We argue in App. A that reasonable values for energetic pulsars are $n = 1.5 \pm 0.5$ and $M \sim 100 \text{ GeV} - 10 \text{ TeV}$.

The overall normalization is more difficult to derive because neither the initial rotational energy nor the conversion efficiency are known for most pulsars. Currently, models can only estimate W_0 to an order of magnitude with significant theoretical uncertainties [35]. In App. A, we derive that, assuming a constant pulsar time scale $\tau = 1 \text{ kyr}$ for all pulsars in the ATNF catalog [28], the distribution of pulsar initial rotational energies $W_0 \equiv 10^p \text{ erg}$ satisfies a log-normal distribution with $\bar{p} \approx 49$ and $\sigma_p \approx 1$ which gives the average $\bar{W}_0 \approx 10^{50} \text{ erg}$. If we use $\tau = 10 \text{ kyr}$, the same analysis gives $\bar{p} \approx 48$, $\sigma_p \approx 1$, and $\bar{W}_0 \approx 10^{49} \text{ erg}$. If the age of a pulsar is known independently, then the initial rotational energy can be estimated more robustly. For example, the Crab pulsar is associated with the SN1054 supernova explosion and has $\tau \approx 0.7 \text{ kyr}$ and $W_0 \approx 5.3 \times 10^{49} \text{ erg}$.

Let us now discuss the conversion coefficient η . The energy density near the surface of the pulsar is dominated by the magnetic field and the spin-down luminosity is dominated by the magnetic dipole radiation. In most PWNe the energy density is believed to be particle dominated, i.e. at large distances from the neutron star most of the energy outflow has been converted to particles and $\eta \sim 1$ at this stage (see, e.g., [36] for a discussion of the Crab PWN). However, these particles do not immediately escape to the ISM but are trapped inside the PWN by its magnetic field where they can lose a significant fraction of their energy. In App. A, we estimate $\eta \sim 0.1$ due to cooling of the particles before they escape into the ISM. Based on the discussion above, we find that the average energy in electrons and positrons $\eta W_0 \sim 10^{49} \text{ erg}$ is reasonable. This value is model dependent and can vary greatly from one pulsar to another.

The density of electrons propagated from a pulsar to the Earth can be found by substituting the source function $Q(\mathbf{x}, E, t)$ into Eq. (9)

$$\rho(\mathbf{x}, E, t) = \frac{b(E_0)}{b(E)} \frac{1}{(4\pi\lambda)^{3/2}} e^{-\frac{\mathbf{x}^2}{4\lambda}} Q(E_0), \quad (18)$$

where parameter λ is defined in Eq. (11) and E_0 is the initial energy of the electrons that cool down to E in time t

$$E_0 = \frac{E}{1 - E b_0 t}. \quad (19)$$

The density in Equation (18) has a cutoff at the cooling break, $E = \frac{1}{b_0 t}$, since $Q(E_0) \rightarrow 0$ for $E_0 \rightarrow \infty$.

For a density ρ of relativistic particles, the flux is defined as

$$F = \frac{c}{4\pi} \rho. \quad (20)$$

The time evolution of the flux from a single pulsar is shown in Fig. 1. At early times, the electrons haven't had enough time to diffuse to the observer and the flux is exponentially suppressed. At later times, the flux grows until the diffusion distance $\sqrt{4D(E)t}$ is similar to the distance from the pulsar to the Earth. After that the flux decreases as the electrons diffuse over a larger volume. The cutoff moves to lower energies due to cooling of electrons.

For energies much smaller than the cooling break, we can neglect energy losses. In this case, $E_0 \approx E$, $\lambda \approx D(E)t$ and Equation (18) reduces to

$$\rho(\mathbf{x}, E, t) = \frac{1}{(4\pi D(E)t)^{3/2}} e^{-\frac{\mathbf{x}^2}{4D(E)t}} Q(E). \quad (21)$$

Assuming that $\mathbf{x}^2 \ll 4D(E)t$, the flux for $E \ll \frac{1}{b_0 t}$ is

$$F(E) = \frac{c}{4\pi} \frac{Q_0}{(4\pi D_0 t)^{3/2}} E^{-n-\frac{3}{2}\delta}. \quad (22)$$

In general, the flux that we add to the backgrounds to fit the data can be effectively parameterized by three numbers: the normalization, the index at low energies, and the cutoff energy. From the right hand side of Eqs. (17) and (22) we find that these three parameters correspond to at least 8 parameters describing the pulsar and the ISM. In particular, the propagated index n_a is a linear combination of n and δ , $n_a = n + \frac{3}{2}\delta$, the propagated cutoff is $E_{\text{cut}} = \frac{1}{b_0 t}$, and the normalization depends on η , W_0 , M , D_0 , and t . In order to fix this degeneracy, as a matter of convenience, we choose $D_0 = 3 \times 10^{28} \text{ cm}^2 \text{ s}^{-1}$, $\delta = 0.4$, $b_0 = 1.6 \times 10^{-16} \text{ GeV}^{-1} \text{ s}^{-1}$, $W_0 = 10^{50} \text{ erg}$,

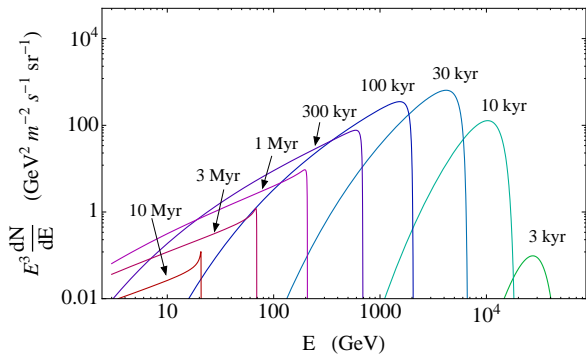


FIG. 1: Time evolution of e^+e^- flux on the Earth from a pulsar at a distance of 1 kpc with $\eta W_0 = 3 \times 10^{49}$ erg, an injection index $n = 1.6$, and an injection cutoff $M = 10$ TeV. The diffusion and energy losses are described in Sec. II A. We assume the delta-function approximation for the emission from the pulsar, $Q(\mathbf{x}, E, t) = Q(E)\delta(\mathbf{x})\delta(t)$. The flux from a young pulsar (the 3 kyr curve on the right) has an exponential suppression because the electrons haven't had enough time to diffuse from the pulsar to the Earth. The cutoff moves to the left due to cooling of electrons and becomes sharper. After reaching a maximal value, the flux decreases since the electrons diffuse over a large volume.

$M = 10$ TeV. With this choice, our fit to the e^+e^- data will determine n , η , and t . If some of the parameters are known independently, e.g., the propagation model, the energy losses, the age of the pulsar etc., this approach becomes more constrained and more predictive. As shown in Figure 2, the expected flux from a pulsar with $\eta W_0 \approx 3 \times 10^{49}$ erg, $n = 1.6$, distance 0.3 kpc, and age 200 kyr, reproduces the positron fraction measured by *PAMELA* and is good fit to the cosmic-ray electron spectrum measured by *ATIC*, *Fermi*, and *HESS* below ~ 1 TeV. This suggests that the anomaly in the e^+e^- flux could be due to a single pulsar. However, given the considerable number of known nearby, energetic pulsars [28], it is unlikely that the flux from any single pulsar is significantly larger than the flux from all such pulsars. In the next section, we will derive the expected flux of electrons and positrons from a collection of pulsars.

III. FLUX FROM A COLLECTION OF PULSARS

In this Section, we derive the e^+e^- flux from a continuous distribution of pulsars and compare it with the predicted flux from the pulsars in the ATNF catalog [28].

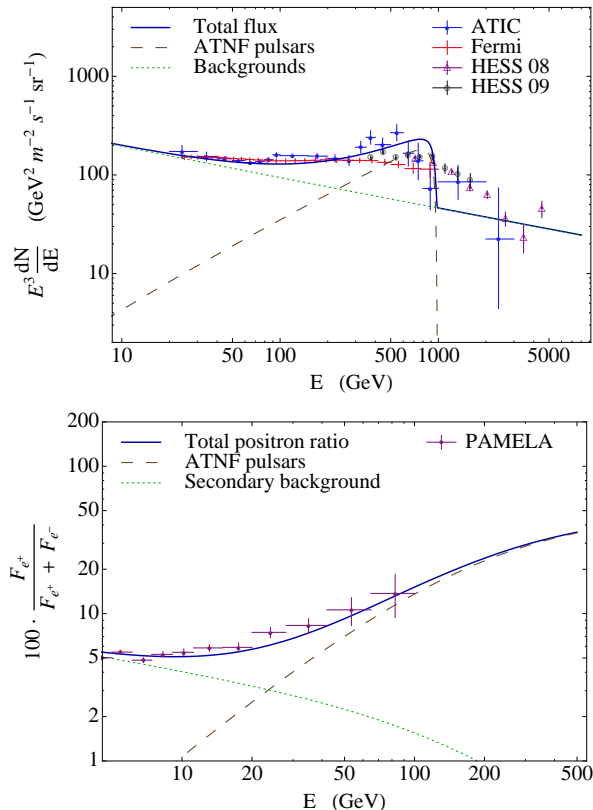


FIG. 2: Electron and positron flux from a single pulsar together with a primary background $\sim E^{-3.3}$ and a secondary background $\sim E^{-3.6}$. The pulsar is at a distance of 0.3 kpc. It has $\eta W_0 = 2.2 \times 10^{49}$ erg, age of 200 kyr, injection index and cutoff $n = 1.6$ and $M = 10$ TeV. The propagation parameters are described in Sec. II A. The cutoff $M \gg 1$ TeV results in a significant bump around 1 TeV which is consistent with the *ATIC* data. For a smaller injection cutoff $M \sim 1$ TeV, the flux from the pulsar takes the form of a power law with an exponential cutoff that can be used to fit the *Fermi* and *PAMELA* data (see, e.g., [37]).

A. Flux derivation

We assume that pulsars are homogeneously distributed in the Galactic plane and are born at a constant rate N_b [35]. The “continuous” distribution of pulsars is defined as the average of all possible realizations of pulsar distributions. This results in a source function constant in time, localized in the vertical direction, and homogeneous in the Galactic plane

$$Q_{\text{distr}}(\mathbf{x}, E, t) = J_0 E^{-n} e^{-\frac{E}{M}} \delta(z) \quad (23)$$

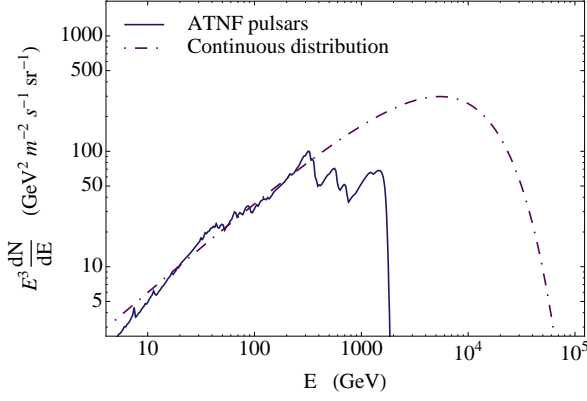


FIG. 3: The expected spectrum from the continuous flux distribution and that from pulsars in the ATNF catalog pulsar [28]. The latter is calculated using $\eta = 0.065$, $n = 1.5$, and a pulsar time scale $\tau = 1$ kyr for each pulsar. This last fact, in conjunction with its spin-down age and current spin-down luminosity, is used to calculate each pulsar's initial rotational energy through Eq. (29). We also use the value of the propagation parameters given in Sec. II A. Several hundred pulsars contribute below 300 GeV and the continuous distribution provides a good approximation for these energies. Above 300 GeV, there are only ~ 10 contributing pulsars, and the observed flux in this energy range is strongly dependent on their individual properties. The reason for the significant discrepancy between these two curves above 2 TeV has to do with the actual local distribution of pulsars versus the averaged flux seen by many observers in the Galaxy, as discussed in Sec. III B.

with the normalization constant

$$J_0 = \frac{\eta W_0}{\Gamma(2-n)M^{2-n}} \frac{N_b}{A_{\text{Gal}}}, \quad (24)$$

where A_{Gal} is the area of the Galactic plane. Since the diffusion distance of these electrons is significantly smaller than the distance from the Earth to the edge of the Galactic plane [35] ($x_{\text{diff}} < 10$ kpc), we can neglect the effects of having an edge at a finite distance.

Using the general Green function in Equation (12), the flux of electrons from this distribution is

$$F = \frac{c}{4\pi} \int d^3\mathbf{x}_0 \int dE_0 \int dt_0 G(\mathbf{x}, E, t; \mathbf{x}_0, E_0, t_0) \cdot Q(\mathbf{x}_0, E_0, t_0). \quad (25)$$

Integrating over t_0 and \mathbf{x} , we obtain

$$F(E) = \frac{c}{4\pi b(E)} \int_E^\infty dE_0 \frac{1}{\sqrt{4\pi\lambda(E, E_0)}} J_0 E_0^{-n} e^{-\frac{E_0}{M}}, \quad (26)$$

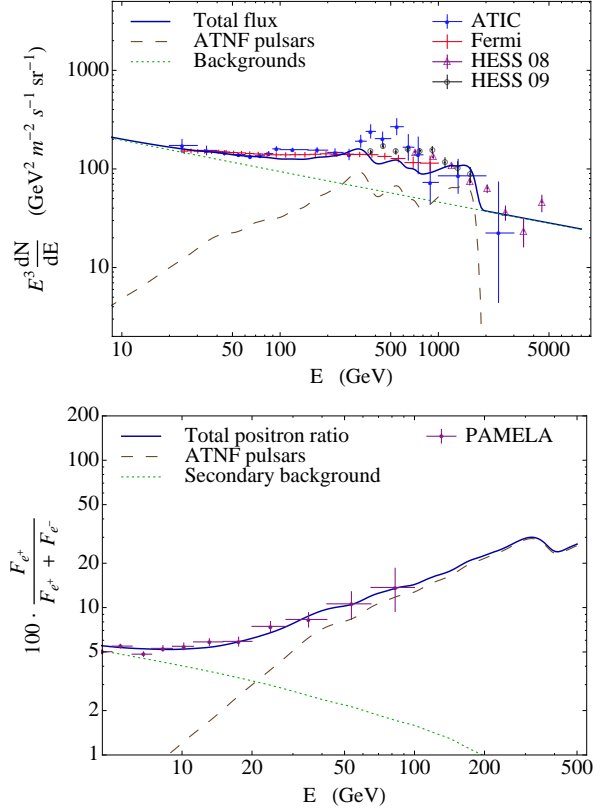


FIG. 4: The predicted flux from pulsars in the ATNF catalog calculated using the same procedure as in Fig. 3 but accounting for spatial variations of energy losses as described in App. B. The assumed backgrounds are the same as in Fig. 2.

where λ is defined in Eq. (11). This flux can be rewritten as

$$F_{\text{distr}}(E) = \frac{c}{4\pi} \frac{J_0}{\sqrt{4\pi b_0 D_0}} I_{\frac{E}{M}} E^{-n-(\delta+1)/2}, \quad (27)$$

where

$$I_{\frac{E}{M}} = \int_1^\infty dx \sqrt{\frac{1-\delta}{1-x^{\delta-1}}} x^{-n} e^{-\frac{E}{M}x}, \quad (28)$$

for example, if $E \ll M$, $\delta = 0.4$, and $n = 1.5$, then $I_{\frac{E}{M}} \approx 3$.

As in the case of a single pulsar flux, the number of parameters we need to fit the data is much smaller than the number of parameters characterizing the flux from a collection of pulsars. In this case, the index of the observed flux and the normalization can be found from Eq. (27). For example, the index of the flux at low energies $n_a = n + (1 + \delta)/2$. Formally, the cutoff in this case is equal to the injection cutoff M , but for an actual distributions of pulsar the expected cutoff is lower and

is determined by the age of the youngest pulsar within the diffusion distance from the observer – as derived in Sec. III B. If we break the degeneracy by picking a particular propagation model, we can constrain the properties of the pulsar distribution. The opposite is also true, by choosing some properties of the pulsars one can constrain the properties of the ISM – as demonstrated in App. C.

In order to break the degeneracy we fix the ISM properties as in Sec. II C. To calculating the flux from the pulsars in the ATNF catalog we use the following toy model. We assume that every pulsar has injection index $n = 1.5$ and conversion efficiency $\eta = 0.065$ (these values are chosen to fit the low energy electron and positron data in Fig. 4). We choose an injection cutoff $M = 10$ TeV for every pulsar (for smaller values of M the features at high energies will be less sharp, since the injection cutoff is not as abrupt as the cooling break). In order to estimate the initial rotational energy, we assume that for each pulsar, the spin-down time scale is $\tau = 1$ kyr. Then we use Eq. (A4) to express the initial rotational energy, $\mathcal{E}_0 \equiv W_0$, in terms of the current spin-down luminosity $\dot{\mathcal{E}}$ and the pulsar age $t \gg \tau$

$$W_0 \approx \dot{\mathcal{E}} \frac{t^2}{\tau}. \quad (29)$$

The result is shown in Fig. 3, and the relative normalization between this spectrum and that of the continuous distribution described above depends on the pulsar birth rate N_b , or, to be more precise, on the local value of the pulsar birth rate. In order to have a good agreement between the two curves for energies 30 – 300 GeV, we require $N_b \approx 1.8 \text{ kyr}^{-1}$, assuming a Milky Way radius $R_{Gal} = 20$ kpc [35]. For energies below 30 GeV, we find that the main contribution to e^+e^- flux comes from the pulsars with age $t > 10$ Myr. These pulsars typically have a very low spin-down luminosity and therefore are difficult to observe (in the ATNF catalog there are very few pulsars with the spin-down luminosities $\dot{\mathcal{E}} < 10^{31}$ erg). In Fig. 4, we apply to this spectrum the Gaussian smearing expected to result from spatial variations in energy losses depending on the path of the electrons – as derived in App. B. As one can see, this provides a very good fit to the *PAMELA*, *Fermi*, and *HESS* data - but does not reproduce the ATIC bump

Determining the flux of e^+e^- from the actual distribution of pulsars using a more realistic model is extremely difficult because every pulsar has its own independent parameters (e.g. W_0 , η , τ). Thus, we may choose several thousands of parameters in order to fit less than a

hundred of data points (which can be fitted by a flux parameterized by three parameters only). Moreover, as we discussed in the Introduction, these thousands of parameters refer to PWNe sufficiently old that their electrons have had enough time to diffuse to the Earth. These PWNe have already disappeared and therefore cannot be observed directly – making it impossible to directly constrain these parameters observationally. The large number of pulsars and the impossibility to derive their individual properties suggests a statistical method is needed to study the e^+e^- flux they produce. At small energies, a lot of pulsars contribute to the observed flux on Earth and therefore the properties of an individual pulsar are unimportant. In this case, the flux should be well approximated by some average curve – as demonstrated in Fig. 3. In this estimate we included all pulsars with ages $t > 15$ kyr and use the delta-function approximation of source functions, $Q(\mathbf{x}, E, t) = Q(E)\delta(\mathbf{x})\delta(t)$ (Sec. II). The choice of the lower cutoff on the age of the pulsars is motivated by the fact that young pulsars, such as the Vela pulsar, usually have a PWN and therefore their electrons haven't escaped yet into the ISM. At high energies only a few young pulsars contribute and the deviation from the average curve may be large. The presence of features at high energies may serve as a signature of a collection of pulsars that can distinguish them from a dark matter or single pulsar origin for these electrons.

B. Statistical cutoff

As shown in Fig. 3, the expected flux from a continuous distribution of pulsar increases with energy until a break at $E \sim M = 10$ TeV, whereas the predicted flux from pulsars in the ATNF database has a cutoff at 2 TeV. This discrepancy is due to the rare events when a young pulsar is very close to the observer. Since electrons lose energy during propagation, high energy electrons must come from young pulsars and the cutoff energy is determined by the age of the youngest pulsar sufficiently close to the observer so that the electrons have enough time to diffuse through the ISM. We will call the average such cutoff a “statistical” cutoff.

To estimate the statistical cutoff, we consider a collection of pulsars and choose an observation point. The statistical cutoff at this point is the maximal cooling break energy for the flux from these pulsars. In this distribution, the youngest pulsar whose electrons can reach the observation point has an age T and diffusion distance

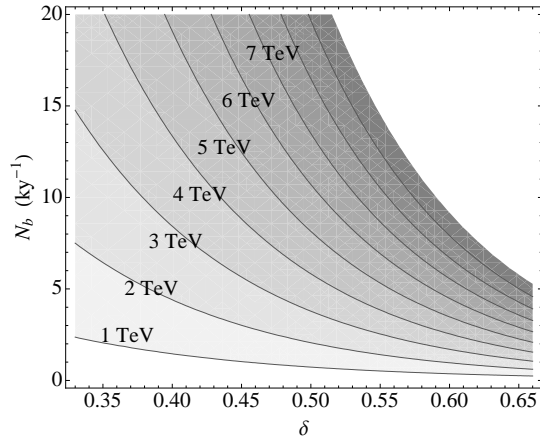


FIG. 5: Statistical cutoff as a function of the diffusion index and the birth rate of pulsars in the galaxy. The cutoff in e^+e^- flux from pulsars is determined by the age of the youngest pulsar within the diffusion distance from the Earth. The average such cutoff is a universal quantity that depends on the properties of ISM (the energy losses and the diffusion coefficient) and on the pulsar birth rate, but it is insensitive to the properties of the injection spectrum from the pulsars. We assume $D_0 = 100 \text{ pc}^2 \text{ kyr}^{-1}$ and $b_0 = 5 \cdot 10^{-6} \text{ GeV}^{-1} \text{ kyr}^{-1}$.

R. For a given pulsar birth rate N_b , we estimate M_{stat} by demanding that there is at least one pulsar within R younger than T . Therefore, we have a system of three equations for the three unknowns R , T and M_{stat} :

$$M_{\text{stat}} = \frac{1}{b_0 T}, \quad (30)$$

$$R^2 = 4D(M_{\text{stat}})T, \quad (31)$$

$$N_b T \frac{\pi R^2}{A_{\text{Gal}}} = 1. \quad (32)$$

Solving this system of equations, we find

$$M_{\text{stat}} = \left(\frac{4\pi D_0 N_b}{b_0^2 A_{\text{Gal}}} \right)^{\frac{1}{2-\delta}}. \quad (33)$$

Assuming $R_{\text{Gal}} = 20 \text{ kpc}$, $D_0 = 10^{-4} \text{ kpc}^2 \text{ kyr}^{-1}$, and $b_0 = 5 \times 10^{-6} \text{ GeV}^{-1} \text{ kyr}^{-1}$, we get

$$M_{\text{stat}} = (4 \times 10^5 N_b)^{\frac{1}{2-\delta}} \text{ GeV}, \quad (34)$$

where N_b is in units of kyr^{-1} . In Fig. 5, we show the statistical cutoff as a function of N_b and the diffusion index δ . This calculation should be viewed as a rough estimate, with the actual flux from the distribution of real pulsars having a cutoff that differs by as much as an order of magnitude. Additionally, it is possible that current data is missing a feature at high energies ($E \gtrsim 2 \text{ TeV}$) due to poor statistics.

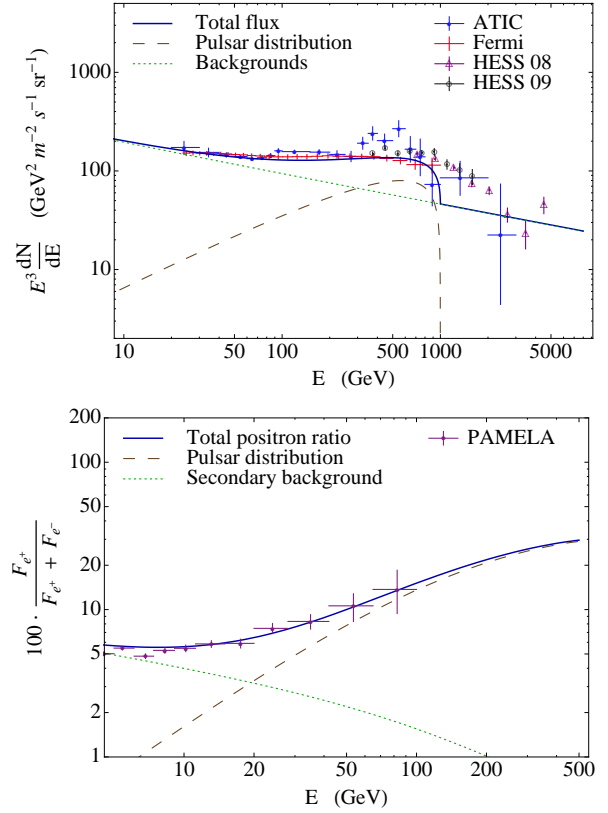


FIG. 6: The flux from a continuous distribution of pulsars. The parameters are chosen to fit the *Fermi* and *PAMELA* data points, $\eta W_0 = 6.5 \times 10^{48} \text{ erg}$ and $n = 1.5$. In this plot, instead of the injection cutoff $M = 10 \text{ TeV}$, we use the statistical cutoff $M_{\text{stat}} = 1 \text{ TeV}$. The backgrounds are the same as in Fig. 2. The propagation parameters are described in Sec. II A.

We note that Eq. (33) can also be used to find the cutoff in the primary background if we assume that it is generated by the supernovae explosions. For instance, for the supernovae rate in the Milky Way $N_{\text{SN}} = 10 \text{ kyr}^{-1}$ and $\delta = 0.4$, it gives the cutoff in the primary background around 3 TeV. Using the same reasoning as above one may expect some features in the spectrum of the primary electrons at several TeV. Below $\sim 1 \text{ TeV}$ we don't expect significant fluctuations in the primary background and the presence of the features should be interpreted as the signature of pulsars.

IV. FLUX FROM DARK MATTER

In this section we briefly review the e^+e^- production from annihilating (decaying) DM and derive that, for a

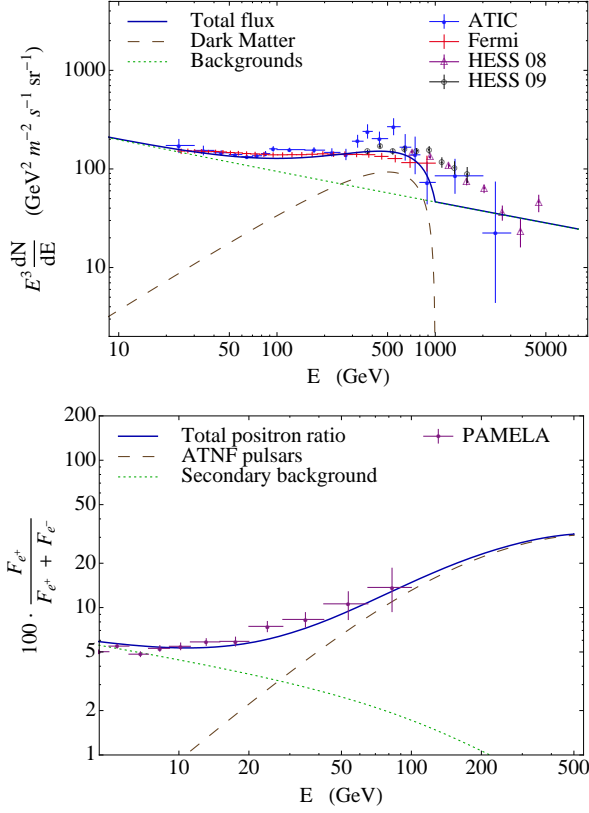


FIG. 7: Flux from DM model in [10] with the annihilation chain $\chi + \chi \rightarrow \phi + \phi \rightarrow 2e^+ + 2e^-$, $M_{\text{DM}} = 1$ TeV and a boost factor $BF \approx 500$. The primary background is $\sim E^{-3.3}$ and the secondary background is $\sim E^{-3.6}$.

large class of DM models, the expected flux has the form of a power law with a universal index $n = 2$ at energies $E \ll M_{\text{DM}}$. If we neglect gradients in the DM density near the Earth, then we approximate any DM contribution as originating from a constant, homogeneous source, which from Eq. (7) gives

$$\rho(E) = \frac{1}{b(E)} \int_E^\infty Q(E') dE'. \quad (35)$$

This equation has an interesting property that for any $Q(E) \sim E^k$ with $k > -1$, the integral is saturated at the upper limit, which in this case is the mass of the DM particle, M_{DM} . For energies $E \ll M_{\text{DM}}$, we can neglect the dependence on E resulting from the lower limit of integration so the index of the electron flux is determined by the index of the energy loss function $b(E) \sim E^2$.

The source function of e^+e^- coming from annihilating dark matter is [38],

$$Q(E) = \frac{1}{2} n_\chi^2 \langle \sigma v \rangle \frac{dN}{dE}, \quad (36)$$

where n_χ is the dark matter number density, $\langle \sigma v \rangle$ is the thermally averaged annihilation cross-section, and dN/dE is the number density of electrons and positrons produced per annihilation event. Here we assume that the DM particle is its own antiparticle otherwise there is an extra factor of 1/2 in Eq. (36). For this source function, the flux of electrons and positrons from annihilating DM is

$$F(E) = \frac{c}{8\pi} \frac{1}{b(E)} n_\chi^2 \langle \sigma v \rangle \int_E^M \frac{dN}{dE'}(E') dE'. \quad (37)$$

If the integral in this equation is saturated at $E_* \lesssim M_{\text{DM}}$, then for $E \ll E_*$ the integral is insensitive to the changes of the lower integration limit and can be approximated by a constant

$$I_{e^\pm} = \int_0^M \frac{dN}{dE'}(E') dE', \quad (38)$$

where I_{e^\pm} is the average number of electrons and positrons produced in an annihilation event. In this case, the only energy dependence in $F(E)$ is from $b(E)$, so $F(E) \sim E^{-2}$. The discussion of the universality of index $n = 2$ with respect to the choice of DM models and DM halo profiles is further discussed in [39] (see also [40][41] for an earlier discussion of the effects of DM substructure).

An important difference between the DM and pulsar models is that the dark matter flux in Eq. (37) has significantly fewer free parameters than the corresponding flux from pulsars. In fact, if we assume that the energy losses in the ISM are well understood and the energy density of dark matter is fixed from the cosmological considerations, there are only two free parameters, M_{DM} and $\langle \sigma v \rangle$, with the specific DM model providing I_{e^\pm} . For a given DM model, M_{DM} is then fixed by the cutoff energy in the observed spectrum and the cross section $\langle \sigma v \rangle$ is fixed by the normalization of the flux. The index of the flux is not parametrically independent, $n \approx 2$. This index is insensitive to the choice of DM model or the DM profile in the host halo but may change significantly in the presence of a large DM subhalo [39]. As an example, we use the DM model in [10] with the annihilation chain, $\chi + \chi \rightarrow \phi + \phi \rightarrow 2e^+ + 2e^-$. DM with the current estimated energy density of $\rho_\chi = 0.3 \text{ GeV cm}^{-3}$ requires $\langle \sigma v \rangle_0 = 3.0 \times 10^{-26} \text{ cm}^3 \text{ s}^{-1}$ at freeze out. One can assume that the current cross section is larger by a boost factor, BF . To fit the ATIC and PAMELA data, we set $M_{\text{DM}} = 1$ TeV, which requires a $BF \sim 500$ to reproduce to observed normalization.

For a decaying DM model, Eq. (37) would be replaced

by

$$F(E) = \frac{c}{4\pi} \frac{1}{b(E)} \frac{n_\chi}{\tau_d} \int_E^M \frac{dN}{dE'} dE', \quad (39)$$

where τ_d is the life-time of the DM particle and $\int \frac{dN}{dE} dE$ is the number of electrons and positrons produced per decay. If we take the same number density and the mass of DM particles as above, then

$$\frac{I}{\tau_d} \sim 5 \times 10^{-27} \text{ s}^{-1}. \quad (40)$$

These estimates agree with the analysis of [42] [43] [44].

V. CONCLUSIONS

In this work, we analyzed the flux of electrons and positrons from a single pulsar, from a continuous distribution of pulsars, from pulsars in the ATNF catalog and from dark matter. Depending on the model parameters and pulsar properties, they all can adequately fit either the *Fermi* and *PAMELA* data or the ATIC and *PAMELA* data. One of the most important question is whether it is possible to distinguish among these possibilities.

In Fig. 8 we compare the expected e^+e^- flux from a single pulsar (Sec. II), pulsars in the ATNF catalog (Sec. III), from a continuous distribution of pulsars (Sec. III), and DM (Sec. IV). We have chosen the parameters of the models such that the fluxes have the same value at 100 GeV, similar indices at low energies, and a cutoff at 2 TeV. At energies below ~ 300 GeV, the fluxes are very similar. We also don't expect to see any differences between these models in the positron ratio below 300 GeV, the upper limit for charge identification in *PAMELA*.

Above 300 GeV, there are substantial differences between the e^+e^- spectrum predicted for these models. However, it should be noted that the sharpness of the cutoff for a single pulsar and for DM is strongly model dependent. If the injection cutoff for a pulsar is ~ 1 TeV, then the cutoff in the observed flux from a single pulsar can be much smoother than if the injection cutoff was higher than the cooling break, in which case its spectrum is indistinguishable from that predicted for a continuous distribution of pulsars. For the DM flux we show a model with only one intermediate particle in the annihilation-decay process. If there are more steps in the annihilation-decay, then the flux has a broader cutoff and, again, may be impossible to distinguish it from either a single pulsar or continuous pulsar distribution

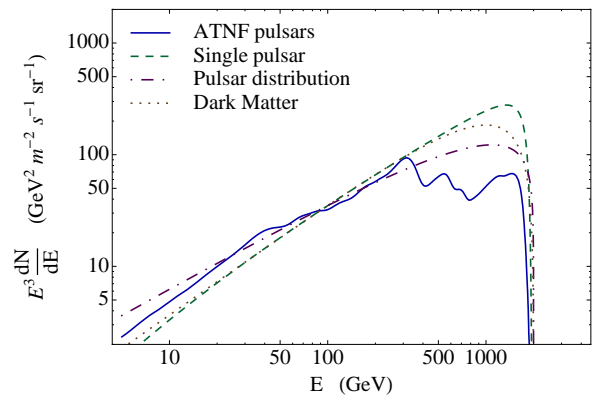


FIG. 8: The fluxes from annihilating dark matter, from a single pulsar, and from a continuous distribution of pulsars can be made similar, depending on the parameters of the models. The flux from a collection of pulsars may have significant deviations from a continuous curve. This property can be used to distinguish the pulsars from the sources producing a featureless spectrum. The flux from pulsars in the ATNF catalog is the same as in Fig. 4. Single pulsar has the age $t = 100$ kyr, distance 0.3 kpc, $\eta W_0 = 9.2 \times 10^{48}$ erg, $n = 1.6$. Continuous pulsar distribution has $N_b = 1.8 \text{ kyr}^{-1}$, $\eta W_0 = 6.5 \times 10^{48}$ erg, $n = 1.5$, $M_{\text{stat}} = 2$ TeV. Dark matter model is the same as in Sec. IV but with $M_{\text{DM}} = 2$ TeV and $BF = 2000$. The ISM properties are the same as in Sec. II A.

origin. Thus, given the significant uncertainties in the pulsar and DM models, it is unlikely that better observations alone can distinguish between a single pulsar and dark matter origin of anomalous e^+e^- flux [26] (a similar conclusion was obtained in [19][45]).

The flux from a discrete collection of pulsars does have a few distinctive features at high energies. The height of these features is model dependent and may be within the error bars of current observations. The presence of these features requires the existence of a few young, nearby, energetic pulsars with an injection cutoff $\gg 1$ TeV. Consequently the absence of such features in the observed e^+e^- spectrum could mean that all young pulsars whose electrons have reached the Earth have had cutoffs $\lesssim 1$ TeV – a strong constraint on the properties of PWNe since, as we discuss in App. A, the PWN around the Vela pulsar has a cutoff in the electron and positron spectrum at an energy $\gg 1$ TeV. An additional smearing of the bumps can be due to spatial variations of the energy losses and the diffusion coefficient. Our general conclusion is that the current electron and positron data are not sufficient to distinguish between the pulsars and the dark matter

and that independent measurements, e.g. the spectrum and morphology of the diffuse Galactic gamma-ray background [45, 46], may be necessary in order to decisively distinguish a pulsar and DM origin of e^+e^- excess.

Acknowledgments. The authors are thankful Gregory Gabadadze, Andrei Gruzinov, Ignacy Sawicki, Jonathan Roberts, and Alex Vikman for valuable discussions. We are especially indebted to Neal Weiner for initiating the project and for numerous discussions and support during all stages of the work. This work is supported in part by the Russian Foundation of Basic Research under grant RFBR 09-02-00253 (DM), by the NSF grants PHY-0245068 (DM) and PHY-0758032 (DM), by DOE OJI grant DE-FG02-06E R41417 (IC), by the NSF Astronomy and Astrophysics Postdoctoral Fellowship under award AST-0702957 (JG).

APPENDIX A: REVIEW OF PULSARS

In this Appendix we review the emission of electrons from pulsars. We assume that this emission is powered by the pulsar's loss of rotational energy. Pulsars are believed to be rotating neutron stars with a strong surface magnetic field [34], and magnetic dipole radiation is believed to provide a good description for its observed loss of rotational energy. A pulsar loses its rotational energy on a characteristic decay time τ defined as

$$\tau = \frac{\mathcal{E}_0}{\dot{\mathcal{E}}_0}, \quad (\text{A1})$$

where \mathcal{E}_0 and $\dot{\mathcal{E}}_0$ are the initial rotational energy and the initial spin-down luminosity, which in the magnetic dipole radiation model are equal to

$$\begin{aligned} \mathcal{E}_0 &= \frac{1}{2} I \Omega_0^2, \\ \dot{\mathcal{E}}_0 &= \frac{B^2 R^6 \sin^2 \alpha}{6c^3} \Omega_0^4, \end{aligned}$$

where Ω_0 is the initial angular velocity, R is the radius of the pulsar, B is the strength of the surface dipole magnetic field, and α is the angle between the rotation axis and the magnetic field axis.

If the energy loss is due to magnetic dipole radiation, then

$$I \Omega \dot{\Omega} = - \frac{B^2 R^6 \sin^2 \alpha}{6c^3} \Omega^4. \quad (\text{A2})$$

Integrating the energy loss equation we get

$$\Omega(t) = \Omega_0 \left(1 + \frac{t}{\tau} \right)^{-\frac{1}{2}}, \quad (\text{A3})$$

$$\dot{\mathcal{E}}(t) = \mathcal{E}_0 \frac{1}{\tau} \left(1 + \frac{t}{\tau} \right)^{-2}. \quad (\text{A4})$$

As a result, the pulsar angular velocity satisfies

$$\frac{\Omega}{2\Omega} = -(t + \tau). \quad (\text{A5})$$

In a more general approach, the time evolution of the angular velocity is described as

$$\dot{\Omega} \sim -\Omega^k, \quad (\text{A6})$$

where k is the braking index, which can be found by measuring the current Ω , $\dot{\Omega}$, and $\ddot{\Omega}$

$$k = -\frac{\Omega \ddot{\Omega}}{\dot{\Omega}^2}. \quad (\text{A7})$$

In this case,

$$\Omega(t) = \Omega_0 \left(1 + \frac{t}{\tau}\right)^{-\frac{1}{k-1}}. \quad (\text{A8})$$

The magnetic dipole radiation corresponds to $k = 3$.

As an example, let us calculate the initial rotational energy of the Crab pulsar using the magnetic dipole approximation and a general braking index. The Crab pulsar is believed to have been produced during SN 1054 supernova explosion. Consequently, the age of the pulsar is known exactly, $t = 955$ yr. In the magnetic dipole approximation, we can use Eq. (A5) and the current values of Ω and $\dot{\Omega}$ [28, 47] to calculate that its pulsar time scale $\tau \approx 0.3$ kyr. Assuming a mass $1.4 M_\odot$, radius $R = 12$ km, and moment of inertia $I = 1.4 \times 10^{45} \text{ g cm}^2$ [34], we derive an initial rotational energy $\bar{W}_0 \approx 3 \times 10^{50}$ erg. Taking into account the measured value of $\dot{\Omega}$ [28], the braking index of the Crab pulsar is $k = 2.5$, which gives $\tau \approx 0.7$ kyr and $W_0 \approx 5.3 \times 10^{49}$ erg.

If the age of the pulsar is not known independently, it is impossible to determine τ and W_0 using its observed properties (from Ω , $\dot{\Omega}$, and $\ddot{\Omega}$ one can only calculate $t + \tau$). In the following, we estimate W_0 by assuming $\tau = 1$ kyr for all pulsars. If so, the initial energy $W_0 \equiv \mathcal{E}_0$ can be found from Eq. (A4) by using the current spin-down luminosity $\dot{\mathcal{E}}$

$$\mathcal{E}_0 = \dot{\mathcal{E}} \tau (1 + t/\tau)^2. \quad (\text{A9})$$

For a general braking index k , this formula takes the form

$$\mathcal{E}_0 = \dot{\mathcal{E}} \tau (1 + t/\tau)^{\frac{k+1}{k-1}} \quad (\text{A10})$$

Using this method to estimate W_0 for all pulsars in the ATNF catalog results in the distribution shown in Fig. 9, using both the magnetic dipole approximation (Eq. (A9)) and a general braking index method (Eq. (A10)). In the magnetic dipole case we took all pulsars within 4 kpc from the Earth and younger than 300 kyr. The reason is that older and more distant pulsars are less luminous and may not be observed for small spin down luminosities, i.e., this introduces a bias towards more energetic pulsars and shifts the distribution toward larger average W_0 . For the general braking index, we used all pulsars with $2 < k < 10$. In both cases, W_0 can be described by a log normal distribution with the average $p = \text{Log}_{10}(W_0/\text{erg}) \approx 49$ and the standard deviation $\sigma_p \approx 1$. The average initial rotational energy in this case is

$$\bar{W}_0 = \frac{1}{\sqrt{2\pi}\sigma_p} \int 10^p e^{-\frac{(p-\bar{p})^2}{2\sigma_p^2}} dp \approx 10^{50} \text{ erg}. \quad (\text{A11})$$

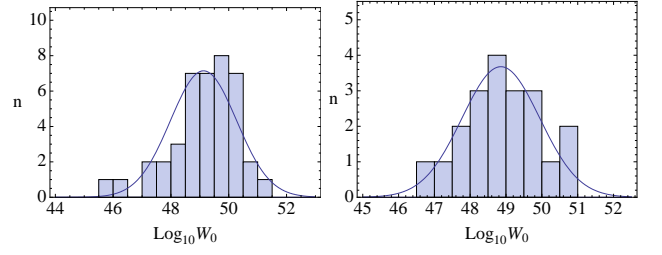


FIG. 9: Left panel has 41 pulsars within 4 kpc from the Earth and younger than 300 kyr. Assuming the braking index 3 and the pulsar time scale $\tau = 1$ kyr we find the average power $p = \text{Log}_{10}(W_0/\text{erg}) = 49.1 \pm 1.1$ with $\chi^2/dof = 1.2$. For the right panel we select the pulsars from the ATNF catalog that have braking index $2 < k < 10$ (there are 20 such pulsars). Assuming the pulsar time scale $\tau = 1$ kyr, these pulsars have $p = 48.9 \pm 1.1$ with $\chi^2/dof = 0.3$. For the pulsar time scale $\tau = 10$ kyr, the left (right) selection of pulsars would have $p = 48.2 \pm 1.1$ (48.1 ± 1.2). Thus, for $\tau = 1$ kyr (10 kyr) the average initial rotational energy is $\bar{W}_0 \approx 10^{50}$ erg (10^{49} erg).

This result is strongly dependent on the chosen value of τ . For example, if $\tau = 10$ kyr, then an analogous calculation gives $\bar{p} \approx 48$, $\sigma_p \approx 1$ and $\bar{W}_0 \approx 10^{49}$ erg. The estimations above agree with the analysis of [35]. It is worth noting that τ likely varies between pulsars.

To estimate η , it is important to understand how the pulsar's magnetic dipole radiation is transferred to the kinetic energy of particles. Since $\dot{\mathcal{E}}$ decays as t^{-2} , most of the rotational energy is lost at early times. A young pulsar is surrounded by several layers [20][25]. Nearest to the neutron star is the magnetosphere, which ends at the light cylinder $R_{LC} \equiv c/\Omega$. The rotating magnetic field creates a strong electric field capable of both producing pairs of particles and accelerating them to relativistic energies. These particles stream away from the light cylinder as a coherent “wind” that ends with a termination shock separating the “wind” zone from the Pulsar Wind Nebula (PWN) which consists of magnetic fields and particles moving in random directions. The PWN in turn is surrounded by a supernova remnant (SNR). A significant PWN exists only at the early times ($t \ll 100$ kyr; [24]).

The spectrum of electrons and positrons in the magnetosphere can be estimated using the spectrum of pulsed γ -ray emission from a pulsar. For the Crab pulsar, model fits to the observed photon spectrum suggests that the spectrum of e^+e^- pairs in its magnetosphere is well-described by a broken power law with an index of 2.0 below $E_{br} \sim 2$ GeV and an index 2.8 between E_{br} and an upper cutoff around 100 GeV [48] (see also [49]). Par-

ticles with this spectrum can *not* reproduce the e^+e^- spectrum observed on Earth, since a break in the injection spectrum at 2 GeV is too low to explain the ATIC and *PAMELA* results, and an index of 2.8 above 2 GeV also does not fit the data. Additionally, the pulsed emission from a pulsar only reflects the energy spectrum of the emitting particles in the emission region, which is not necessarily representative of the spectrum of particles that escape the pulsar magnetosphere along the open field lines and are eventually deposited in the ISM.

These particles are further accelerated before they enter the PWN, most likely at the termination shock between the magnetosphere and the PWN (for a review see, e.g., [50]). Once deposited in the PWN, they are trapped by the PWN's magnetic field until it is disrupted. Observationally, the spectrum of the electrons inside the PWN is found by analyzing their broadband spectrum, which at low photon energies (< 1 GeV) is dominated by synchrotron emission and at higher energies (> 100 GeV) dominated by inverse Compton scattering of electrons off background photons [36]. From the radio spectrum of these objects, it is possible to constrain the spectral shape of the low energy (GeV) electrons which dominate by number the electron population of a PWN. An average index of the electron and positron spectrum can be found using data from the publicly available Catalogue of Galactic SNRs [51], where F-type (or “filled-center”) SNRs are PWNe, S-type are the supernovae shells, and C-type SNRs are a combination of the two. There are 7 F-type SNRs with an average electron index $n_F \equiv 2\alpha + 1 = 1.3 \pm 0.3$. For 21 C-type SNRs the average index is $n_C = 1.8 \pm 0.4$, while 168 S-type SNRs have $n_S = 2.0 \pm 0.3$. It is clear that the spectrum of electrons in supernovae shells is much softer (decreases faster with the energy) than the spectrum in PWNe. In order to explain *PAMELA* positron ratio we need either F-type or, possibly, C-type SNRs because the S-type SNRs are produced by the initial supernovae explosion and don't contain a significant number of positrons.

The broadband spectrum of most PWNe shows a break between the radio and X-ray regimes, believed to correspond to a break in the electron and positron spectrum, most likely the result of synchrotron cooling. Converting the frequency of this break to an electron/positron energy requires knowing the strength of the PWN's magnetic field. An independent estimate of the magnetic field is available for those PWNe with detected inverse Compton emission, since this depends solely on the energy spec-

trum of electrons and positrons in the PWN and known properties of the various background photon fields (e.g. Cosmic Microwave Background and starlight). The best studied example is the Crab Nebula (e.g. [36]), whose broadband photon spectrum suggests an electron spectrum well described by a broken power law with an index $n = 1.5$ below $E_0 \sim 200$ GeV and $n = 2.4$ between E_0 and an upper cutoff $E_{\text{cut}} \sim 10^3$ TeV, the magnetic field in this PWN has a strength of $B \approx 2 \times 10^{-4}$ G, resulting in a ratio of magnetic energy flux to particle energy flux of $\sigma < 0.01$ [36]. For PWNe whose broadband spectrum is not as well determined, the break energy in the electron spectrum is typically derived using the minimum energy assumption ($\sigma = 0.75$; [52]). Using this method and the observational data provided in [52], we estimate a break energy of $\sim 3 - 300$ GeV for the PWNe listed in this paper. It is important to emphasize that this procedure almost certainly overestimate the magnetic field strength inside a PWN since, for most PWN, σ is believed to be $\sigma \ll 0.75$. In this procedure, the inferred break energy E_b is $E_b \propto B_{\text{pwn}}^{-1/2}$, where B_{pwn} is strength of PWN's magnetic field. As a result, the true break energy of electrons and positrons inside the PWNe analyzed above is likely to be at least an order of magnitude higher than the derived value.

The break energy in the electron/positron spectrum of a PWN is expected to vary considerably during the lifetime of a PWN due largely to changes in the strength of the PWN's magnetic field (e.g. [53], [54]). Therefore, the break energy in the spectrum of electrons and positrons injected by the PWN into the surrounding ISM depends strongly on the evolutionary phase of the PWN when this occurs. During the initial free-expansion phase of the PWN's evolution (the Crab Nebula is the prototypical example of such a PWN; [24]), the break energy is expected to increase as $\sim t^{1.6}$ [53, 54]. This phase of the PWN's evolution ends when it collides with the SNR's reverse shock, typically on the order of $\sim 10^4$ years after the supernova explosion. If this holds for the Crab Nebula, its current age of ~ 1000 years and break energy of ~ 200 GeV suggests that, at the time of this collision, the break energy will have risen to ~ 8 TeV. The evolution of the break energy after this collision is more complicated and depends strongly on the properties of the central neutron star, progenitor supernova, and surrounding ISM (see [54] for a more detailed discussion). There is observational evidence that the break energy of older PWN ($> 10^4$ years old) is considerably higher than

that of the Crab Nebula and other young PWNe ($\sim 10^3$ years). The most convincing example comes from a recent analysis of the broadband spectrum (radio to TeV γ -rays) of the Vela PWN (often referred to as “Vela X”), which suggests a break in the electron spectrum of ~ 67 TeV [55]. For the purpose of the work presented here, the exact value of the break is not important as far as it is bigger than ≈ 1 TeV.

Observations indicate that most PWNe are particle dominated, i.e. almost 100% of the spin-down luminosity is transformed into the energy of the particles after the termination shock. However, not all of this energy is eventually deposited in the ISM. We estimate this fraction, η , by first assuming that the spectrum after the termination shock is a power law $Q(E) \sim E^{-n}$ with an index $n < 2$ and a cutoff $E_c \sim 10^3$ TeV. Then, the total energy in electrons is

$$W_{\text{ini}} \sim \int E^{-n} E dE \sim E_c^{2-n}. \quad (\text{A12})$$

If, when the PWN is disrupted, the energy spectrum of electrons in the PWN is E^{-n} below the break at E_{br} and E^{-n_b} with $n_b > 2$ above the break, the total energy in electrons is saturated at E_{br} with

$$W_{\text{fin}} \sim E_{\text{br}}^{2-n}. \quad (\text{A13})$$

The efficiency is therefore

$$\eta = \frac{W_{\text{ini}}}{W_{\text{fin}}} \sim \left(\frac{E_{\text{br}}}{E_c} \right)^{2-n}. \quad (\text{A14})$$

For $n = 1.5$, $E_{\text{br}} = 10$ TeV and $E_c = 10^3$ TeV, this gives the suggested $\eta = 0.1$. This derivation should be viewed as an order of magnitude estimation. A more realistic calculation is extremely complicated and involves the knowledge of the PWN evolution and the actual spectra of particles inside a PWN. Recent work in this field does support an efficiency of $\eta \sim 0.1$ (e.g. [54]).

It should be stressed that, apart from theoretical uncertainties, the parameters of the injection spectrum can vary significantly between pulsars. The initial rotational energy can differ by several orders of magnitude, while the index of the electron spectrum n can vary from 1 to 2. In some cases, it is observed to vary inside the PWN of a single pulsar. The upper cutoff M , as we have seen in the examples of Crab and Vela pulsars, can vary at least between ~ 100 GeV and ~ 10 TeV.

APPENDIX B: SPATIAL VARIATION IN ENERGY LOSSES

As we have discussed, an important signature of the flux from the pulsars is the presence of a number of bumps at the cooling break energies

$$E_i = \frac{1}{bt_i}, \quad (\text{B1})$$

where t_i 's are the ages of the pulsars. The existence of these bumps is based on the assumption that the energy losses depend only on the travel time and not their path. In reality, the energy loss coefficient depends on the position, since the densities of the star light and IR photons vary in space. In this case, there is no simple solution for Eq. (7), though one can still find the average energy loss and its standard deviation by averaging the energy losses over random paths.

As a useful simplification we will consider separately diffusion in space and energy losses. Our motivation is that a particle detected with energy E has an energy close to E during most of the propagation time (i.e. the cooling time from E_0 to E is saturated by the final energy E). Consequently, the diffusion coefficient for all particles detected with energy E can be approximated by $D(E)$. If so, the probability to propagate from a source at (x_0, t_0) to an observer at (x_1, t_1) is given by the Green function

$$G(x_1, t_1; x_0, t_0) = \frac{1}{(4\pi D(E)\Delta t)^{3/2}} e^{-\frac{\Delta x^2}{4D(E)\Delta t}}. \quad (\text{B2})$$

In order to find the energy loss averaged over paths, it is useful to rewrite this Green function in terms of the path integral

$$G(\mathbf{x}_1, t_1; \mathbf{x}_0, t_0) = \int Dx(t) e^{-S[x(t)]}, \quad (\text{B3})$$

where the action is

$$S[x(t)] = \int \frac{1}{4D(E)} \dot{x}^2 dt \quad (\text{B4})$$

with the boundary conditions $x(t_0) = x_0$ and $x(t_1) = x_1$.

In general, the average of a functional $\mathcal{O}[x(t)]$ over paths is

$$\langle \mathcal{O} \rangle = \frac{\int Dx(t) \mathcal{O}[x(t)] e^{-S[x(t)]}}{\int Dx(t) e^{-S[x(t)]}}. \quad (\text{B5})$$

Integrating the energy loss

$$\frac{dE}{dt} = -b(x)E^2 \quad (\text{B6})$$

along a path $x(t)$, we find

$$\frac{1}{E_1} - \frac{1}{E_0} = \int_{t_0}^{t_1} b(x) dt. \quad (\text{B7})$$

The functional that we will study is

$$\mathcal{O}[x(t)] = \int_{t_0}^{t_1} b(x) dt. \quad (\text{B8})$$

The expression in the numerator of (B5) is

$$\begin{aligned} \text{Num} &= \int Dx(t) \int_{t_0}^{t_1} dt' b(x(t')) e^{-S[x(t)]} \\ &= \int_{t_0}^{t_1} dt' \int Dx(t) b(x(t')) e^{-S[x(t)]}. \end{aligned} \quad (\text{B9})$$

If we define $x' = x(t')$, then all the paths can be represented as a path from x_0 to x' , the integral over all x' and the path from x' to x_1

$$\begin{aligned} \text{Num} &= \int_{t_0}^{t_1} dt' \int_{x_0}^{x'} Dx(t) \int_{x'}^{x_1} Dx(t) \\ &\quad \cdot b(x(t')) e^{-S[x(t)]} \end{aligned} \quad (\text{B10})$$

$$\begin{aligned} &= \int_{t_0}^{t_1} dt' \int dx' G(x_1, t_1; x', t') \\ &\quad \cdot b(x') G(x', t'; x_0, t_0). \end{aligned} \quad (\text{B11})$$

The resulting expression resembles the first order perturbation theory: there is a propagation from x_0 to x' , insertion of an operator at x' and a propagation from x' to x_1 .

The average energy loss can be estimated with (B11) and the Green function in (B2). Taking $E_0 \rightarrow \infty$ in (B7), we find that the average cooling break energy for a given pulsar is

$$\begin{aligned} \langle \frac{1}{E_{\text{br}}} \rangle &\equiv \langle \mathcal{O} \rangle = \left(\int_{t_0}^{t_1} dt' \int dx' G(x_1, t_1; x', t') b(x') \right. \\ &\quad \cdot G(x', t'; x_0, t_0) \Big) / G(x_1, t_1; x_0, t_0). \end{aligned} \quad (\text{B12})$$

The standard deviation is

$$\sigma_{\mathcal{O}} = \sqrt{\langle \mathcal{O}^2 \rangle - \langle \mathcal{O} \rangle^2}. \quad (\text{B13})$$

The average $\langle \mathcal{O}^2 \rangle$ for the functional (B8) can be computed analogously to (B12)

$$\begin{aligned} \langle \mathcal{O}^2 \rangle &= 2 G^{-1}(x_1; x_0) \\ &\quad \int_{t_0}^{t_1} dt' \int dx' \int_{t'}^{t_1} dt'' \int dx'' G(x_1; x'') \\ &\quad \cdot b(x'') G(x''; x') b(x') G(x'; x_0), \end{aligned}$$

where we assume that x' is at t' and x'' is at t'' . The factor of two is the usual $n!$ for the time-ordered path integrals.

The relative standard deviation of the cooling break energy is

$$\frac{\Delta E}{E} = \frac{\sigma_{\mathcal{O}}}{\langle \mathcal{O} \rangle}. \quad (\text{B14})$$

Using the energy densities of starlight and IR photons from [31] we find the relative smearing in the energy

$$\frac{\Delta E}{E} \approx 0.053 \cdot \left(\frac{E}{1 \text{ TeV}} \right)^{-1/3}. \quad (\text{B15})$$

At 1 TeV the smearing is about 5%, at 100 GeV it is 11%, and 24% at 10 GeV. The flux from the ATNF pulsars with this smearing is shown in Fig. 4. At low energies the flux becomes very smooth but at high energies the bumps are still visible. We also notice that at high energies the relative width of the bumps is larger than the ratio in (B15). Thus, even if the experimental energy resolution is about 10 – 15%, we should be able to see the bumps.

APPENDIX C: CONSTRAINING PULSARS AND ISM PROPERTIES

If we assume that the anomalies in *Fermi*, ATIC and *PAMELA* data are due to pulsars, we can use these results to constrain the properties of ISM and pulsars. The problem is that the flux depends on both the properties of the ISM and the injection spectrum from pulsars. As we discuss in Sections II and III, the ISM can be described by three parameters D_0 , δ , b_0 and the injection from a distribution of pulsars can be described by five parameters W_0 , η , n , M , and N_b . Obviously, the three parameters of the observed flux (the normalization, the index, and the cutoff) cannot constrain all eight parameters, but they can constrain some combinations of parameters. These constraints may be very useful if combined with results from other experiments, such as the observations of protons, heavy nuclei, or diffuse gamma rays.

Another concern is the reliability of constraints coming from the local e^+e^- flux. Ideally, we would like to constrain the parameters in the models, but since the local distribution of pulsars is fundamentally random in nature, there is a possibility that we can only constrain the properties of particular pulsars without getting any information about the general population. The reason why we think our approach is sensible is the following.

At high energies, the flux from pulsars will depend significantly on the properties of individual pulsars (and we can use this region to prove that the observed flux is due to pulsars), but at low energies the flux is well approximated by the continuous distribution flux and the properties of individual pulsars are relatively unimportant. Thus, we propose using the observed spectrum at intermediate energies $100 \text{ GeV} < E < 500 \text{ GeV}$ as a testing ground to study the general (or averaged) properties of e^+e^- injection from pulsars.

In the following we will fit the continuous distribution flux derived in Eq. (27) to the *Fermi* and *PAMELA* data simultaneously. In these fits we substitute the usual pulsar injection cutoff $M \sim 10 \text{ TeV}$ by the propagated (or statistical) cutoff M_{stat} and treat it as a fit parameter. The other fit parameters are $b_0 = (0.5 - 3) \times 10^{-16} \text{ GeV}^{-1} \text{ s}^{-1}$ (these values are based on the energy densities of radiation and magnetic field within few kpc from the Earth), $\delta = (0.3 - 0.6)$ [30]. The injection index $n \approx (1 - 2)$ and the conversion efficiency $\eta W_0 \sim 10^{48} - 10^{49} \text{ erg}$ are discussed in App. A. In the fits we use $D_0 = 100 \text{ pc}^2 \text{ kyr}^{-1}$, $N_b = 1.8 \text{ kyr}^{-1}$ and $R_{\text{Gal}} = 20 \text{ kpc}$. The best fit parameters are: $\delta = 0.48$, $b_0 = 1.05 \times 10^{-16} \text{ GeV}^{-1} \text{ s}^{-1}$, $\eta W_0 = 4.9 \times 10^{48} \text{ erg}$, $n = 1.7$, and $M_{\text{stat}} = 1.0 \text{ TeV}$. The corresponding fluxes are shown in Fig. 6.

In Fig. 10 we plot the 68%, 95% and 99% CL of these parameters. Every contour plot is obtained by varying two parameters while keeping the rest fixed at their best fit value. We can see that for any value of the energy loss coefficient b_0 within the region chosen, there is a value of diffusion index δ that can provide a fit within 95% CL. Additionally, a higher value of n suggests a lower value of δ , in agreement with the calculation of the e^+e^- flux from a continuous distribution of pulsars where we expect that $F \sim E^{-n-(\delta+1)/2}$ from Eq. (27). Assuming a high value for the injection index ($n \geq 1.6$), the *Fermi* and *PAMELA* data could be fitted by a relatively large region of values of the propagation parameters ($0.3 \leq \delta \leq 0.6$ and $b_0 \leq 3 \times 10^{-16} \text{ GeV}^{-1} \text{ s}^{-1}$). On the other hand, values of $n < 1.3$ don't seem to give a very good fit to the data, with any combination of propagation parameters. Also if the total energy converted to e^+e^- is smaller than $2 \times 10^{48} \text{ erg}$, then for a pulsar birth rate of 1.8 per kyr regardless of the value of n the *Fermi* and *PAMELA* data can't be explained by the continuous distribution of pulsars.

To show the robustness of our procedure we applied the same analysis for two different backgrounds, a power law

Pulsar Distribution	b_0	δ	n	η
Cont. Dist. B1	0.5-3.0	0.30-0.60	1.35-1.95	0.025-0.11
Cont. Dist. B2	0.5-3.0	0.30-0.60	1.40-1.95	0.020-0.085
4kpc Pulsars B1	0.5-2.4	0.30-0.60	1.25-1.80	0.025-0.14
4kpc Pulsars B2	0.5-2.0	0.30-0.60	1.15-1.95	0.020-0.13

TABLE I: Table of best-fit parameters within 95% CL. The values of b_0 are in units of $10^{-16} \text{ GeV}^{-1} \text{ s}^{-1}$. In the first two lines, the ranges are given for a continuous distribution of pulsars. In the last two lines the equivalent ranges are given for the distribution of all Pulsars within 4 kpc. B1 and B2 stand for the two backgrounds, simple power law and more realistic-conventional background [56]. We assume the mean initial rotational energy $W_0 = 10^{50} \text{ erg}$.

background (B1) and a more conventional background used in [56] (B2). In Table I, we present the 95% C.L. allowed region of values of the averaged ISM and averaged pulsar properties, using the two different backgrounds for the continuous pulsar distribution used. Alternatively, we used the properties of pulsars in the ATNF database with estimated distances $d < 4 \text{ kpc}$. We present in Table I the derived constraints in the ISM averaged properties and universal pulsar properties n and ηW_0 .

Better data on the flux of the high energy e^+e^- and on the pulsar birth rate will make this analysis more successful in confining the parameter space that is relevant for the pulsar scenario. Tighter constraints of the backgrounds and the parameters of propagation through the ISM, will be needed to confine the properties of pulsars themselves.

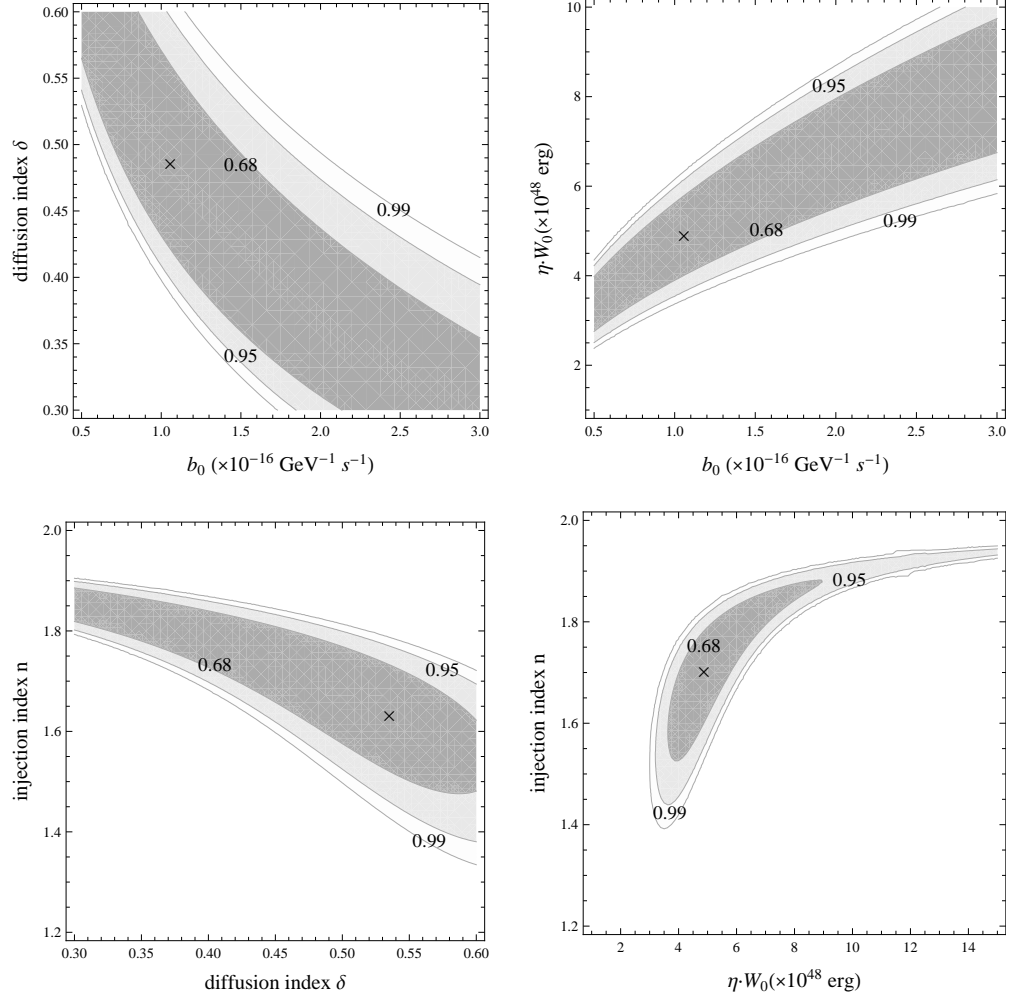


FIG. 10: The fits of the continuous distribution flux to the ATIC and *PAMELA* data. The best fit parameters are: $\delta = 0.48$, $b_0 = 1.05 \times 10^{-16} \text{ GeV}^{-1} \text{ s}^{-1}$, $\eta W_0 = 4.9 \times 10^{48} \text{ erg}$, $n = 1.7$, and $M_{\text{stat}} = 1.0 \text{ TeV}$. The contours show the confidence levels relative to the best fit, $\sigma^2 = (\chi^2 - \chi_*^2)/dof$, where χ_*^2 is the chi squared for the best fit parameters.

-
- [1] J. Chang *et al.*, “An excess of cosmic ray electrons at energies of 300.800 GeV,” *Nature* **456** (2008) 362–365.
- [2] O. Adriani *et al.*, “Observation of an anomalous positron abundance in the cosmic radiation,” [arXiv:0810.4995 \[astro-ph\]](#).
- [3] **H.E.S.S.** Collaboration, F. Aharonian *et al.*, “The energy spectrum of cosmic-ray electrons at TeV energies,” *Phys. Rev. Lett.* **101** (2008) 261104, [arXiv:0811.3894 \[astro-ph\]](#).
- [4] **H.E.S.S.** Collaboration, F. Aharonian *et al.*, “Probing the ATIC peak in the cosmic-ray electron spectrum with H.E.S.S.,” [arXiv:0905.0105 \[astro-ph.HE\]](#).
- [5] **The Fermi LAT** Collaboration, A. A. Abdo *et al.*, “Measurement of the Cosmic Ray e^+ plus e^- spectrum from 20 GeV to 1 TeV with the Fermi Large Area Telescope,” [arXiv:0905.0025 \[astro-ph.HE\]](#).
- [6] I. Cholis, L. Goodenough, and N. Weiner, “High Energy Positrons and the WMAP Haze from Exciting Dark Matter,” [arXiv:0802.2922 \[astro-ph\]](#).
- [7] L. Bergstrom, T. Bringmann, and J. Edsjo, “New Positron Spectral Features from Supersymmetric Dark Matter - a Way to Explain the PAMELA Data?,” *Phys. Rev.* **D77** (2008) 103520, [arXiv:0808.3725 \[astro-ph\]](#).
- [8] M. Cirelli, M. Kadastik, M. Raidal, and A. Strumia, “Model-independent implications of the e^+ , e^- , anti-proton cosmic ray spectra on properties of Dark Matter,” [arXiv:0809.2409 \[hep-ph\]](#).
- [9] I. Cholis, L. Goodenough, D. Hooper, M. Simet, and N. Weiner, “High Energy Positrons From Annihilating Dark Matter,” [arXiv:0809.1683 \[hep-ph\]](#).
- [10] N. Arkani-Hamed, D. P. Finkbeiner, T. Slatyer, and N. Weiner, “A Theory of Dark Matter,” (2008) , [arXiv:0810.0713 \[hep-ph\]](#).
- [11] P.-f. Yin *et al.*, “PAMELA data and leptonically decaying dark matter,” [arXiv:0811.0176 \[hep-ph\]](#).
- [12] K. Hamaguchi, E. Nakamura, S. Shirai, and T. T. Yanagida, “Decaying Dark Matter Baryons in a Composite Messenger Model,” [arXiv:0811.0737 \[hep-ph\]](#).
- [13] C.-R. Chen, K. Hamaguchi, M. M. Nojiri, F. Takahashi, and S. Torii, “Dark Matter Model Selection and the ATIC/PPB-BETS anomaly,” [arXiv:0812.4200 \[astro-ph\]](#).
- [14] F. A. Aharonian, A. M. Atoyan, and H. J. Voelk, “High energy electrons and positrons in cosmic rays as an indicator of the existence of a nearby cosmic tevatron,” *Astron. Astrophys.* **294** (1995) L41–L44.
- [15] T. Kobayashi, Y. Komori, K. Yoshida, and J. Nishimura, “The most likely sources of high energy cosmic-ray electrons in supernova remnants,” *Astrophys. J.* **601** (2004) 340–351, [arXiv:astro-ph/0308470](#).
- [16] D. Hooper, P. Blasi, and P. D. Serpico, “Pulsars as the Sources of High Energy Cosmic Ray Positrons,” *JCAP* **0901** (2009) 025, [arXiv:0810.1527 \[astro-ph\]](#).
- [17] H. Yuksel, M. D. Kistler, and T. Stanev, “TeV Gamma Rays from Geminga and the Origin of the GeV Positron Excess,” [arXiv:0810.2784 \[astro-ph\]](#).
- [18] S. Profumo, “Dissecting Pamela (and ATIC) with Occam’s Razor: existing, well-known Pulsars naturally account for the ‘anomalous’ Cosmic-Ray Electron and Positron Data,” [arXiv:0812.4457 \[astro-ph\]](#).
- [19] K. Ioka, “A Gamma-Ray Burst for Cosmic-Ray Positrons with a Spectral Cutoff and Line,” [arXiv:0812.4851 \[astro-ph\]](#).
- [20] M. J. Rees and J. E. Gunn, “The origin of the magnetic field and relativistic particles in the Crab Nebula,” *Mon. Not. Roy. Astron. Soc.* **167** (1974) 1–12.
- [21] P. A. Caraveo, G. F. Bignami, A. DeLuca, S. Mereghetti, A. Pellizzoni, R. Mignani, A. Tur, and W. Becker, “Geminga’s Tails: A Pulsar Bow Shock Probing the Interstellar Medium,” *Science* **301** (2003) 1345–1348.
- [22] G. G. Pavlov, D. Sanwal, and V. E. Zavlin, “The pulsar wind nebula of the Geminga pulsar,” *Astrophys. J.* **643** (2006) 1146–1150, [arXiv:astro-ph/0511364](#).
- [23] B. M. Gaensler *et al.*, “The Mouse That Soared: High Resolution X-ray Imaging of the Pulsar-Powered Bow Shock G359.23-0.82,” *Astrophys. J.* **616** (2004) 383–402, [arXiv:astro-ph/0312362](#).
- [24] B. M. Gaensler and P. O. Slane, “The Evolution and Structure of Pulsar Wind Nebulae,” *Ann. Rev. Astron. Astrophys.* **44** (2006) 17–47, [arXiv:astro-ph/0601081](#).
- [25] C. F. Kennel and F. V. Coroniti, “Confinement of the Crab pulsar’s wind by its supernova remnant,” *Astrophys. J.* **283** (1984) 694.
- [26] J. Hall and D. Hooper, “Distinguishing Between Dark Matter and Pulsar Origins of the ATIC Electron Spectrum With Atmospheric Cherenkov Telescopes,” [arXiv:0811.3362 \[astro-ph\]](#).
- [27] **FERMI-LAT** Collaboration, D. Grasso *et al.*, “On possible interpretations of the high energy electron-positron spectrum measured by the Fermi Large Area Telescope,” [arXiv:0905.0636 \[astro-ph.HE\]](#).
- [28] R. N. Manchester, G. B. Hobbs, A. Teoh, and M. Hobbs, “The ATNF Pulsar Catalogue,” [arXiv:astro-ph/0412641](#).
<http://www.atnf.csiro.au/research/pulsar/psrcat>.

- [29] M. S. Longair, *High-energy astrophysics*. Cambridge University Press, 1992.
- [30] A. W. Strong, I. V. Moskalenko, and V. S. Ptuskin, “Cosmic-ray propagation and interactions in the Galaxy,” *Ann. Rev. Nucl. Part. Sci.* **57** (2007) 285–327, [arXiv:astro-ph/0701517](#).
- [31] T. A. Porter and A. W. Strong, “A new estimate of the Galactic interstellar radiation field between 0.1 microns and 1000 microns,” [arXiv:astro-ph/0507119](#).
- [32] V. L. Ginzburg and S. I. Syrovatskii, *The Origin of Cosmic Rays*. Pergamon, Oxford, 1964.
- [33] S. I. Syrovatskii, “The Distribution of Relativistic Electrons in the Galaxy and the Spectrum of Synchrotron Radio Emission,” *Astr. Zh.* **36** (1959) 17.
- [34] S. L. Shapiro and S. A. Teukolsky, *Black Holes, White Dwarfs, and Neutron Stars*. John Wiley & Sons, 1983.
- [35] C.-A. Faucher-Giguere and V. M. Kaspi, “Birth and Evolution of Isolated Radio Pulsars,” *Astrophys. J.* **643** (2006) 332–355, [arXiv:astro-ph/0512585](#).
- [36] F. A. Aharonian and A. M. Atoyan, “On the mechanisms of gamma radiation in the Crab Nebula,” *Mon. Not. Roy. Astron. Soc.* **278** (1996) 525–541.
- [37] D. Malyshev, “On discrepancy between ATIC and Fermi data,” [arXiv:0905.2611 \[astro-ph.HE\]](#).
- [38] G. Bertone, D. Hooper, and J. Silk, “Particle dark matter: Evidence, candidates and constraints,” *Phys. Rept.* **405** (2005) 279–390, [arXiv:hep-ph/0404175](#).
- [39] M. Kuhlen and D. Malyshev, “ATIC, PAMELA, HESS, Fermi and nearby Dark Matter subhalos,” [arXiv:0904.3378 \[hep-ph\]](#).
- [40] M. Pohl, “Cosmic-ray electron signatures of dark matter,” [arXiv:0812.1174 \[astro-ph\]](#).
- [41] D. Hooper, A. Stebbins, and K. M. Zurek, “The PAMELA and ATIC Excesses From a Nearby Clump of Neutralino Dark Matter,” [arXiv:0812.3202 \[hep-ph\]](#).
- [42] I. Cholis, G. Dobler, D. P. Finkbeiner, L. Goodenough, and N. Weiner, “The Case for a 700+ GeV WIMP: Cosmic Ray Spectra from ATIC and PAMELA,” [arXiv:0811.3641 \[astro-ph\]](#).
- [43] J. Hisano, M. Kawasaki, K. Kohri, and K. Nakayama, “Neutrino Signals from Annihilating/Decaying Dark Matter in the Light of Recent Measurements of Cosmic Ray Electron/Positron Fluxes,” [arXiv:0812.0219 \[hep-ph\]](#).
- [44] J. Liu, P.-f. Yin, and S.-h. Zhu, “Prospects for Detecting Neutrino Signals from Annihilating/Decaying Dark Matter to Account for the PAMELA and ATIC results,” [arXiv:0812.0964 \[astro-ph\]](#).
- [45] J. Zhang *et al.*, “Discriminate different scenarios to account for the PAMELA and ATIC data by synchrotron and IC radiation,” [arXiv:0812.0522 \[astro-ph\]](#).
- [46] S. Ando, “Gamma-ray background anisotropy from galactic dark matter substructure,” [arXiv:0903.4685 \[astro-ph.CO\]](#).
- [47] A. G. Lyne, R. S. Pritchard, and F. G. Smith, “23 years of Crab pulsar rotational history,” *MNRAS* **265** (1993) 1003–1012.
- [48] A. K. Harding, J. V. Stern, J. Dyks, and M. Frackowiak, “High-Altitude Emission from Pulsar Slot Gaps: The Crab Pulsar,” [arXiv:0803.0699 \[astro-ph\]](#).
- [49] **The MAGIC** Collaboration, E. Aliu *et al.*, “Detection of pulsed gamma-rays above 25 GeV from the Crab pulsar,” [arXiv:0809.2998 \[astro-ph\]](#).
- [50] J. Arons, “Pulsars as Gamma-Rays Sources: Nebular Shocks and Magnetospheric Gaps,” *Space Sci. Rev.* **75** (1996) 235–255.
- [51] D. A. Green, “A Revised Galactic Supernova Remnant Catalogue,” [arXiv:0905.3699 \[astro-ph.HE\]](#). to appear in the Bulletin of the Astronomical Society of India.
- [52] R. A. Chevalier, “Young core collapse supernova remnants and their supernovae,” *Astrophys. J.* **619** (2005) 839–855, [arXiv:astro-ph/0409013](#).
- [53] S. P. Reynolds and R. A. Chevalier, “Evolution of pulsar-driven supernova remnants,” *Astrophys. J.* **278** (1984) 630–648.
- [54] J. D. Gelfand, P. O. Slane, and W. Zhang, “A Dynamical Model for the Evolution of a Pulsar Wind Nebula inside a Non-Radiative Supernova Remnant,” [arXiv:0904.4053 \[astro-ph.HE\]](#).
- [55] **H.E.S.S.** Collaboration, F. Aharonian *et al.*, “First detection of a VHE gamma-ray spectral maximum from a Cosmic source: H.E.S.S. discovery of the Vela X nebula,” *Astron. Astrophys.* **448** (2006) L43–L47, [arXiv:astro-ph/0601575](#).
- [56] A. A. Abdo *et al.*, “Discovery of TeV gamma-ray emission from the Cygnus region of the galaxy,” *Astrophys. J.* **658** (2007) L33–L36, [arXiv:astro-ph/0611691](#).